SAND2020-13702C

Structural Dynamic Measurements using High-Speed X-Ray Digital Image Correlation

Daniel P. Rohe, Enrico C. Quintana, Bryan L. Witt, and Benjamin R. Halls

Sandia National Laboratories*
P.O. Box 5800 - MS0557
Albuquerque, NM 87123
dprohe@sandia.gov

ABSTRACT

Optical test methods, such as scanning laser Doppler vibrometry or Digital Image Correlation (DIC) have many benefits over traditional instrumentation for structural dynamics measurements, such as providing full-field measurements of surfaces without mass-loading the test object. However, one significant drawback is their limitation to line-of-sight measurements; if the test object has internal components of interest, purely external measurements will not likely be adequate to characterize it. The novel use of X-ray images with DIC was recently demonstrated as a viable technique for quasi-static measurements. This work investigates extending this technique to perform high-speed X-ray DIC to capture structural dynamic measurements. A specialized test setup was created to facilitate simultaneous high-speed capture of both visible light and X-ray images for a comparative DIC analysis. Proof-of-concept testing was performed on a simple academic plate structure and a comparison of the results from both systems is presented.

Keywords: X-ray; Radiography; DIC; Modal;

1 Introduction

As structural dynamics testing evolves, test personnel are often asked to perform more challenging measurements to help validate complex models of the structure of interest. Optical approaches such as Laser Doppler Vibrometry (LDV) and Digital Image Correlation (DIC) have significantly improved the ability to acquire large quantities of data in a short amount of time, which can facilitate rapid test throughput. If the component is too small or light to attach instrumentation such as accelerometers, optical approaches can provide a non-contact measurement. At-temperature testing can be performed without worrying about the effects on the sensor's sensitivity.

Still, with current optical techniques, there remains the requirement of line-of-sight to the test article, and for many aerospace structures, the interesting dynamics derive from motion of large internal substructures rather than the shell or skin deformations. Historically, this has required supplementing an optical test with several internal instrumentation locations, which are typically applied during the build-up of the test article, and can often be placed in suboptimal positions due to clearance and cabling constraints within the unit.

Sandia National Laboratories has begun investigating high-speed X-ray imaging in conjunction with DIC as a way to charac-

*Sandia National Laboratories is a multimission laboratory managed and operated by National Technology & Engineering Solutions of Sandia, LLC, a wholly owned subsidiary of Honeywell International Inc., for the U.S. Department of Energy's National Nuclear Security Administration under contract DE-NA0003525.

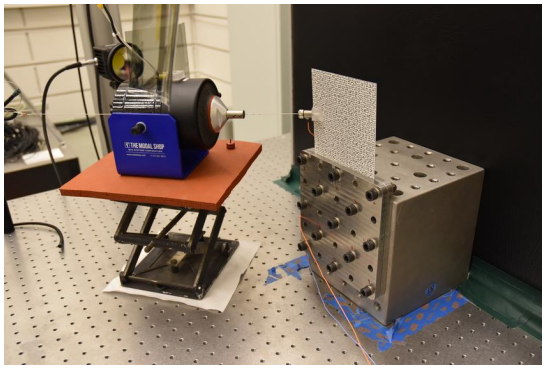

Figure 1: Test article mounted to a vibration cube.

terize the motion of internal components while maintaining the advantages of the optical testing techniques [1]. This paper documents the first attempt to use X-ray imaging to perform experimental modal analysis. The X-ray imaging was performed simultaneously with traditional visible light imaging to compare and contrast the two imaging techniques. Digital Image Correlation (DIC) was used to extract motions from the images, and then modes were fit to the DIC responses.

2 Test Design

2.1 Test Article

As this is a first attempt to extract motions from a part using X-ray imaging, a relatively simple part was desired. A clamped flat aluminum plate was selected as a test article for this work, as it exhibits out-of-plane motions and rich dynamics. Additionally, a plate can be made flexible enough to ensure visible displacements. Finally, the single surface allowed visible light and X-ray imaging techniques to measure the same degrees of freedom, allowing a more direct comparison between the two techniques. The dimensions of the plate in this work were 5 inches $\times$ 6 inches $\times$ 1/16 inch.

The plate was provided a fixed boundary condition by clamping it along one edge to a vibration cube using thick steel plates. One inch of the plate was clamped, leaving a 5 $\times$ 5 inch section of the plate exposed. One bolt was placed through the plate itself to try to provide a more uniform clamping pressure. The test article and all imaging equipment were mounted to an optical table. The test article and mounting configuration are shown in Figure 1.

2.2 Test Setup

Simultaneous measurements with comparable imaging geometry were desired between the X-ray and visible light systems to ensure a meaningful comparison between the two techniques. This meant compromising both imaging systems rather than setting up one system optimally and having the other system off to the side. The test setup was therefore designed to have a nominally 30° stereo angle, with each imaging system offset 7.5° from the plate's perpendicular direction. 3D modeling was initially performed to understand how the test setup might fit within the constraints of the laboratory space, one iteration of which is shown in Figure 2.

Once the approximate test geometry was identified, a Matlab-based Optical Planning Tool [2] was used to identify lenses and apertures that would provide an adequate view of the part given the constraints set by the modeling. This provided an estimate of the number of pixels across the part and could be used to define an optimal speckle size, which was approximately 1 mm.

2.3 Excitation

The test article was excited using a modal shaker (Modal Shop Model 2025E with QSC PLD4.3 power amplfier) to provide the most controllable excitation. The effects of the shaker on the part were thoroughly investigated using a scanning laser doppler vibrometer test prior to the actual image-based measurement.

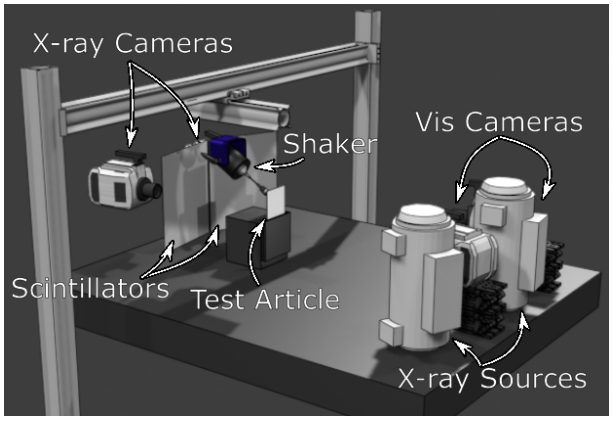

Figure 2: Computer model of one iteration of the test design showing X-ray tubes and scintillators, X-ray and Visible Light cameras, and an early shaker excitation strategy.

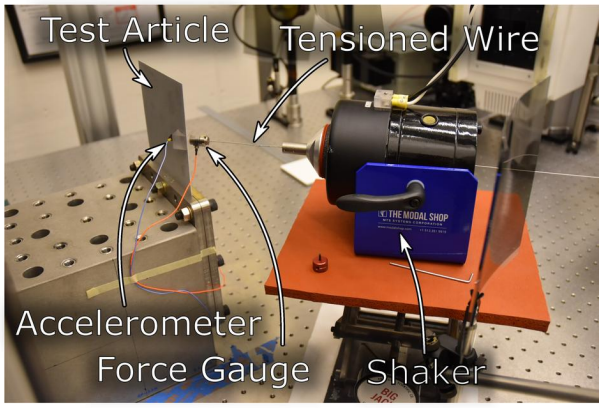

Figure 3: Shaker and attachment configuration.

A tensioned wire connected the shaker to the relatively thin plate to reduce stinger modes as much as possible, as the wire has much lower bending stiffness than a traditional stinger rod. Still, due to the relatively thin plate, there were some mass loading and stinger effects on the dynamics of the plate. There were also some mild nonlinear effects as forcing level changed due to the clamping joint.

The shaker excited the plate halfway between the clamped and free ends. While larger motions could be obtained if the shaker were attached at the free end, there were also larger mass-loading and stinger effects due to the large (by experimental modal analysis standards) rotations and displacements at the free end of the plate. Conversely, the test setup with the minimum effect of the shaker on the part dynamics had the shaker attachment near the fixed base of the plate. However, with this setup, the motion for a given force would be much lower as the mode shapes tend towards zero motion at the fixed base.

One final consideration was the oblique mounting of the shaker with respect to the part. While for a traditional optical test, the shaker can usually be placed behind the part with respect to the cameras, in this case, X-ray images are integrated over the entire path between the X-ray source and the scintillator, so the concept of "behind" does not exist. To ensure that the shaker was not within the X-ray system's field of view, it had to be placed off to the side of the part, and was therefore mounted on a 45° polycarbonate block and a stinger length of 3 inches was required. To perform the experimental modal analysis, a force gauge and drive point accelerometer were also mounted to the 45° block. This is shown in Figure 3.

A flat-force band-limited pseudorandom excitation was applied to the part. A pseudorandom excitation is used over a true random excitation because fewer measurement frame averages are required, which means a shorter run time for the X-ray sources. When a flat voltage spectrum is applied using a shaker, there will often be force drop-outs at lightly damped modes. However, these frequencies are where most of the motion will be occurring, so applying less force at these frequency lines will result in significantly less displacement of the part. Therefore, a flat-force input spectrum was created by measuring the transfer function between the shaker input voltage and the force measured at the part, and a shaped voltage spectrum was created that would result in a flat force output. The bandwidth of the excitation was 10–1000 Hz.

2.4 Contrast Pattern

All image-based measurement techniques require some kind of contrast across the image from which motion can be extracted, regardless of the technique used to acquire the images. For visible light imaging, a common method of generating a contrast pattern for DIC consists of applying a base coat of white paint followed by black paint or ink speckles. However, for X-ray imaging, contrast is instead created by differences in X-ray absorption along the X-ray's path. In [1], the X-ray contrast was created by depositing "splats" of high-density tantalum material using thermal spray coating. The high-density tantalum splats absorbed more X-rays than the surrounding aluminum, and thus created contrast on the resulting X-ray images.

For this work, alternative speckling approaches were investigated. The goal for this work was to use the same speckle pattern

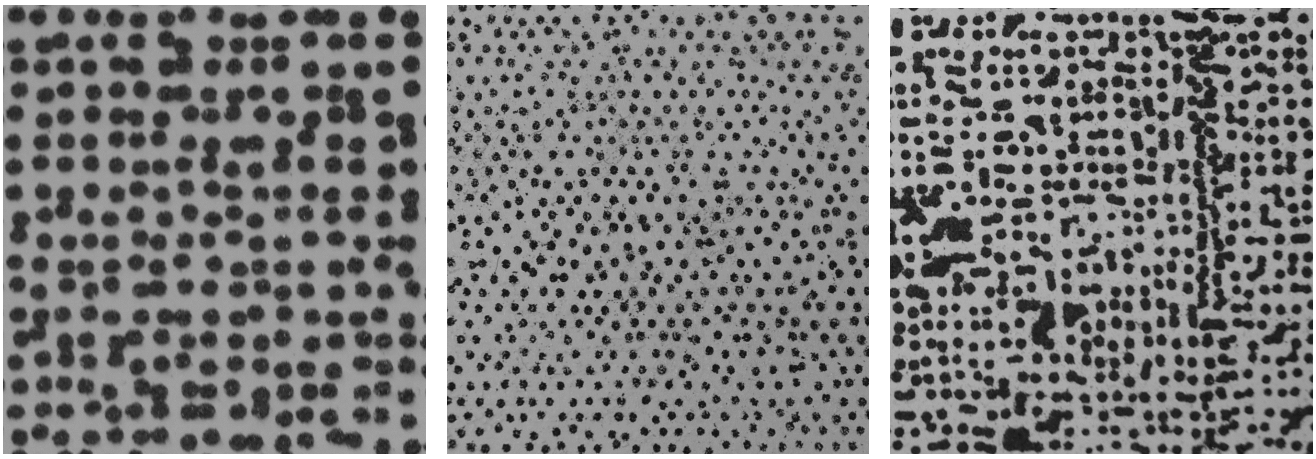

(a) Speckle pattern created using a vinyl mask from a Cricut Maker machine.

(b) Speckle pattern created using a 3D printed mask from a Formlabs Form 2 SLA 3D printer.

(c) Speckle pattern created using a speckle pattern ink-roller from Correlated Solutions

Figure 4: Images of the speckle patterning techniques investigated in this work.

both for visible light and X-ray imaging to ensure differences in the imaging techniques were not conflated with differences in the contrast pattern. Therefore the part was first covered with a flat-white paint prior to the application of a darker color tungsten powder used in this work to create the speckle pattern. Different methods of applying the tungsten powder to the part are described in the following subsections. For all approaches, a coating of hairspray over the speckle pattern was used to seal the tungsten powder in place, with the added benefit of darkening the powder, which added more contrast to the visible light test.

2.4.1 Vinyl Mask

The most successful approach for this work was the use of a Cricut Maker machine to cut holes in a vinyl mask. This mask was then adhered to the part. Spray paint was then sprayed over the masked part to act as an adhesive, and tungsten powder was then sprinkled into the adhesive. After the adhesive paint dried, the mask was removed, leaving just the speckle pattern. An example of this pattern is shown in Figure 4a.

This approach provided the most consistent results of the techniques investigated in this work. One drawback of this approach was that the Cricut Maker machine struggled to cut holes in the vinyl mask smaller than 2 mm, which meant that the 2 mm speckles for this pattern were larger than the optimal 3-5 pixels that is generally recommended for DIC [3]. This speckling technique was ultimately used for the testing described in this paper, but the alternative techniques investigated are also provided for completeness.

2.4.2 3D Printed Mask

Another successful approach was the use of a Formlabs Form 2 SLA 3D printer to print a mask. Unlike the vinyl mask used previously, which was thin and flexible, the 3D printed mask was thicker and more rigid. Therefore, the 3D printed mask was adhered to the part using a glue stick, which was found to be a good adhesive as it sealed the mask to the part so the powder did not seep between the mask and the part, but it also allowed the mask to be peeled off the part without damaging the paint or speckles. This approach is shown in Figure 4b.

This approach provided a reasonably consistent result, with the advantage that the mask holes could be made smaller than with the Cricut machine, more closely matching the optimal 1 mm speckle size. The glue stick adhesive, however, being more viscous than the spray paint did not capture as much powder, so the tungsten powder was less thick, and therefore provided less X-ray contrast.

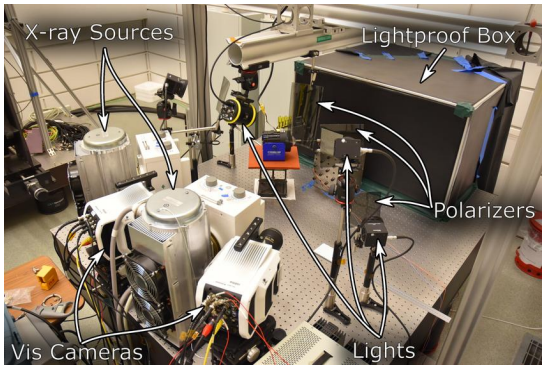

Figure 5: Test setup showing the visible light imaging system, complete with lighting and polarizers. Two X-ray tubes for the X-ray imaging system are also visible.

2.4.3 Ink-roller

A final approach that was successful was to use an ink roller from the Correlated Solutions DIC Speckle Kit to apply paint to the part in a speckle pattern. The tungsten powder was then sprinkled onto the paint. This approach is shown in Figure 4c.

This approach was not very consistent. Obtaining a uniform coating of paint on the roller was difficult, resulting in speckles of non-uniform size. The nominally 1 mm speckles would often spread out and bleed together due to excess paint on the roller. Additionally, the ink roller was not wide enough to cover the whole part in one pass, so the boundary between the roller passes had a different density of speckles depending on how much the passes overlapped each other.

2.5 Imaging and Data Acquisition Systems

2.5.1 Visible Light Imaging System

The visible light imaging system used two Phantom v1212 cameras with Nikon Nikkor 105mm lenses stopped to approximately f/11. Several lights were placed around the part out of the field of view of both imaging systems to provide illumination for the visible light imaging system. Polarizing film was placed in front of each light source, and linear polarizing filters were placed on each lens to cut down on specular reflections from the metal powder. The visible light imaging system is shown in Figure 5.

2.5.2 X-ray Imaging System

Current industrial X-ray machines are generally designed to run continuously for hours at low power (≈4.5 kW). Flash X-ray machines can output much higher powers (≈2.7 GW); however the X-ray system is only on for a few nanoseconds. Structural dynamics measurements will generally operate somewhere between these two extremes.

For this work, a medical X-ray system was adapted for industrial use. A Varex G-292 150 kV rotating anode X-ray tube was used with 80 kW input power capability. The maximum heat capacity of this unit is 445 kJ. X-ray on-times are software limited to protect the X-ray tube. The system has a 1.2 mm focal spot size. The X-ray sources can be seen in Figure 5 next to the high speed cameras from the visible light imaging system.

X-rays emitted by the X-ray source then travel through the part and impact the scintillator. The scintillator converts X-ray photons to visible light photons that can be recorded with a standard high-speed camera. To be useful for structural dynamic measurements, the scintillators must have sufficient light output while also decaying quickly enough to reduce the "motion blur" between frames. The scintillators used in this work are Gadolinium OxySulfide doped with Praseodymium (GOS:Pr), which have a decay time of 3-4 μs and an emission wavelength of 510 nm. The scintillators are mounted to a 0.0625 inch aluminum panel for rigidity, so only the active side is imaged. The scintillators can be seen in Figure 6. Each X-ray source uses a collimator to focus the beam onto its scintillator to ensure, for example, that no X-rays from the right source end up activating the left scintillator. The collimators are visible in Figure 5 and are more clearly shown in Figure 7.

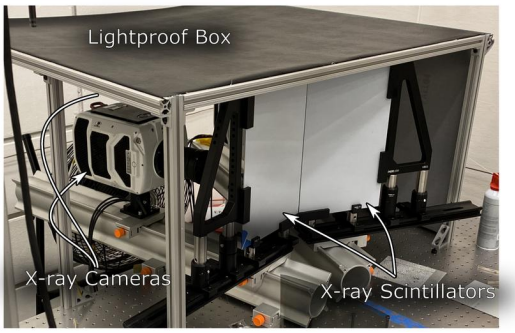

Figure 6: Scintillators used in the X-ray imaging system.

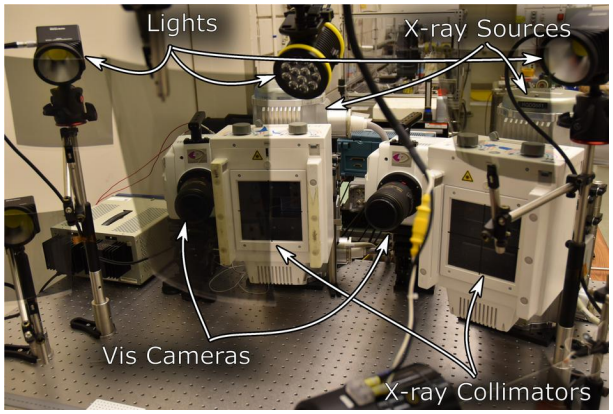

Figure 7: X-ray collimators shown attached to the front of the X-ray sources.

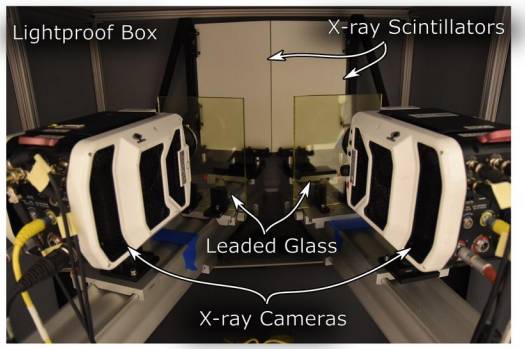

Figure 8: X-ray cameras, leaded glass, and scintillators in the light-proof box.

The photons from the scintillators are captured with Phantom v2511 high-speed cameras with Zeiss Distagon 35mm lenses stopped to f/1.4. A light-proof box was constructed from thick fabric around the scintillators and X-ray cameras in order to prevent the bright light from the visible light portion of the test overwhelming the light from the scintillators. Additionally, a piece of leaded glass was placed in front of the X-ray cameras to protect the camera sensors from direct impingement of X-rays. If an X-ray hits the sensor of the high-speed camera, the impacted pixels will immediately saturate. The leaded glass greatly reduces the frequency and the effect of this occurrence at the expense of reducing some of the light to the camera. The scintillators, leaded glass, and cameras can be seen inside the light-proof box in Figure 8.

2.5.3 Data Acquisition System

The final component of the test is the B+K Lan-XI data acquisition system used to acquire the force and accelerometer measurements at the drive point. The data acquisition system also supplies the shaker excitation using its arbitrary source capabilities. The data acquisition system was generally oversampled by a factor of two compared to the cameras to ensure the signal did not extend past the camera Nyquist frequency, as well as to compensate for small time delays between the camera and data acquisition system.

2.5.4 Timing and Synchronization

All cameras used in the test are synchronized using F-sync to within approximately 50 ns of each other. The data acquisition system was synchronized with the cameras to within one sample. A Standford Research Systems Digital Delay Generator was used to supply the trigger pulses to the various systems in a controlled manner. The X-ray sources were triggered first to allow the rotating anode time to spin up. The cameras and data acquisition system were then triggered to acquire the data. Figure 9

Figure 9: Test overview showing the data acquisition systems and shaker amplifier.

shows the entire test setup, incuding data acquisition system and shaker amplifier.

3 X-ray Image Corrections

While images from a visible light test can be passed as-is into DIC software for analysis, X-ray images should first be modified to improve results.

3.1 Horizontal Flipping of Images

First, to produce a better comparison between visible light and X-ray datasets, the X-ray images are flipped horizontally. This can be done because there is not a "front" or "back" of an X-ray image like there is with a visible light image. All rays go through the entire scene. Therefore, by flipping the image horizontally, we take the scene as imaged by the X-ray cameras (which are on the opposite side of the scintillators as the visible light cameras) and transform it as if it were imaged from the visible light camera side of scintillator.

3.2 Light-field Correction

A second correction process applied to the X-ray images is light-field correction. Due to imperfections or non-uniform lighting in the scintillator, X-ray images may not have uniform brightness even for an empty image. The light-field correction step corrects for this non-uniformity. Light-field images of an empty field of view are captured for a baseline brightness value. When test images are acquired, these are divided by the baseline value on a pixel-by-pixel basis to produce an image with values between 0 and 1, where 1 is as bright as the empty scene and 0 is complete black. These normalized images are then scaled back to 90% of the maximum value of the image ($2^{16} - 1$ for a 16-bit image) and saved as light-field corrected images. This process is shown schematically in Figure 10.

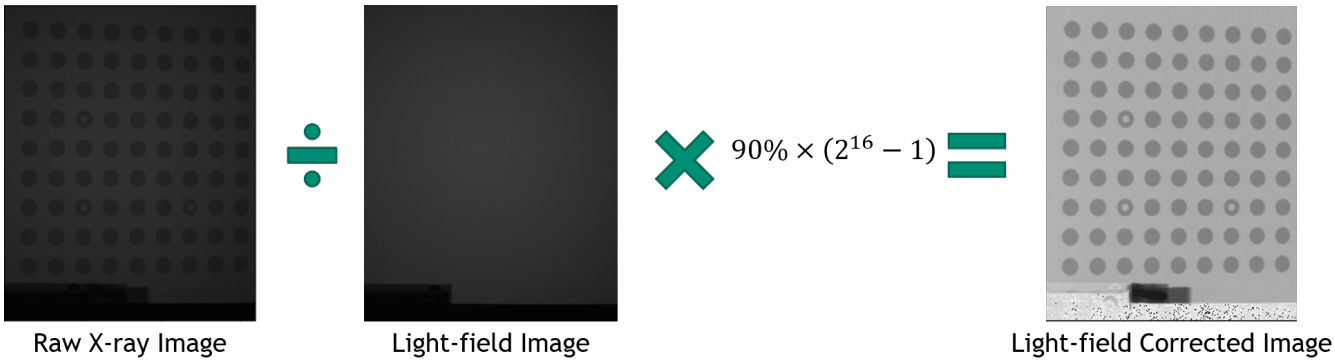

Figure 10: Light-field correction process for a calibration image.

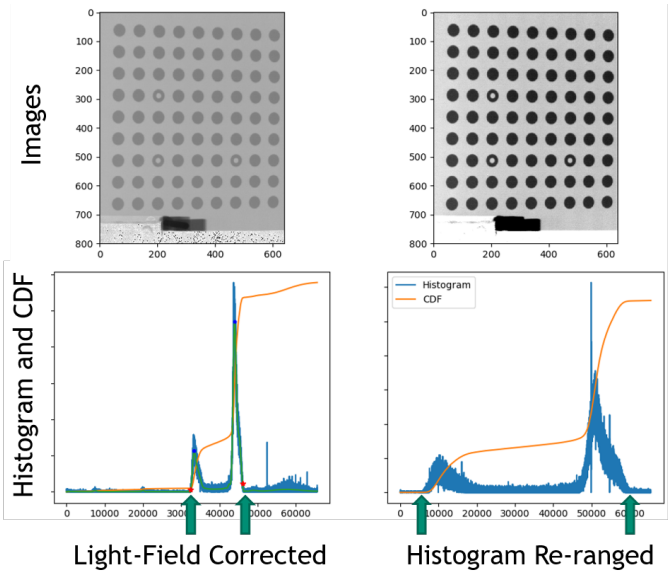

Figure 11: Histogram re-ranging of a calibration image increases the contrast of the image so the dots can be more easily extracted.

3.3 Histogram Re-ranging

The final correction applied to X-ray images is Histogram Re-ranging, which is a process to increase contrast in an image. This process does not generally improve DIC results, as noise is scaled along with the image. However, it can make it easier for calibration routines to find the dots in a calibration target, so this processing step is only performed on the calibration images, as described in Section 5. For a calibration image, the histogram will generally consist of two main peaks, the darker peak will correspond to the "dot grid" that the calibration routine aims to extract from the image. The lighter peak will correspond to the background of the calibration target. The histogram re-ranging process linearly scales pixel intensity so that the dark peak is at 10% of the maximum intensity and the light peak is at 90% of the maximum intensity. Pixels outside this range may clip; however, the calibration routine does not care about these pixels as they are outside the dot grid pattern. The histogram re-ranging process is shown in Figure 11.

4 X-ray Power Study

For the X-ray sources used in this work, the voltage and current supplied to the X-ray source were variable. Generally, the X-ray voltage determines how penetrating the X-rays are and governs image contrast between the sample background and the contrasting features (either calibration target dots or speckles). The current determines how many X-ray photons are emitted which, in combination with the properties of the scintillators, governs image brightness and image noise. The power, which is

the product of these two quantities, determines how much heat is generated and thus the run-time of the system. Therefore, it is useful to determine optimal X-ray power settings for a given test, to optimize image quality and system run-time.

The metrics chosen to optimize are the contrast ratio *CR* between light background and dark speckles or calibration dots, as well as the signal to noise ratio *SNR* defined as the mean intensity divided by the standard deviation of a section of the light background. The final image metric to optimize is then defined as a product of these two metrics $(CR-1)\times SNR$.

The X-ray system was optimized both for a static test (i.e. a single image; no consideration on the length of time the system must run) for both calibration target (for the standard calibration, see Section 5) and test article (for the hybrid calibration, see Section 5.4) as well as for a dynamic test (i.e. system settings that could be maintained continuously for 5 seconds) for the test article. The static test power parameters could be used for calibration images, while the dynamic test power settings would need to be used for the actual modal test.

To optimize the parameters, a set of images was acquired at various voltage and current settings. For the static images, power settings were varied between 40–120 kV and 100–500 mA. For the dynamic images, the current was limited to 100 mA by the X-ray software in order to achieve a 5 second run time, and the voltage was varied between 100–150 kV. For the static tests, 100 images were averaged together to reduce noise in the final image. For the dynamic tests, only 10 images were averaged together, as that was the expected number of frame averages in the modal test.

Tables 1–3 show the image metrics for the cases investigated and Figures 12–14 show crops of representative images. The best combined metric for the static test images was found at 80 kV and 500 mA for both the calibration target and the speckled test piece. The final calibration target imaging parameters were stepped down to 70 kV and 500 mA to ensure that the X-ray sources were not damaged over a large number of calibration images. The best combined metric for the dynamic test images of the speckled test piece was found at 130 kV and 100 mA. The dynamic results discussed in Section 6 were acquired with these settings.

Even with optimal power settings, the visible light images had significantly more contrast than the X-ray images. Figure 15 shows a histogram comparison between representative X-ray and visible light images.

Table 1: Test matrix and image quality metric for static images of the calibration target.

		Voltage: kV								
		40	50	60	70	80	90	100	110	120
Current: mA	100	0	2	9	14	18	22	24	27	27
	200	2	12	19	27	33	34	35	39	38
	320	7	19	30	40	37	44	43	42	40
	400	10	24	37	42	45	46	43	41	38
	500	12	30	45	46	49	47	44	42	35

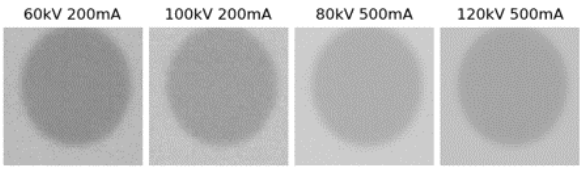

Figure 12: Representative image crops of a single dot on the calibration target corresponding to the boxed values in Table 1

Table 2: Test matrix and image quality metric for static images of the speckled plate.

		Voltage: kV								
		40	50	60	70	80	90	100	110	120
Current: mA	100	0	18	42	65	95	84	117	138	119
	200	12	47	89	128	124	122	134	138	136
	320	21	77	142	120	148	157	149	145	143
	400	31	102	153	156	159	163	160	136	137
	500	41	123	156	170	180	152	145	137	131

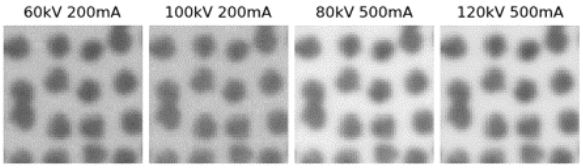

Figure 13: Representative image crops of the speckled plate corresponding to the boxed values in Table 2

Table 3: Test matrix and image quality metric for dynamic images of a the speckled plate.

	Voltage: kV					
	100	110	120	130	140	150
100 mA	31	40	49	65	62	61

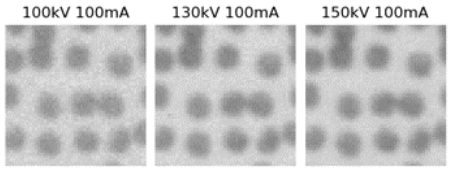

Figure 14: Representative image crops of the speckled plate corresponding to the boxed values in Table 3

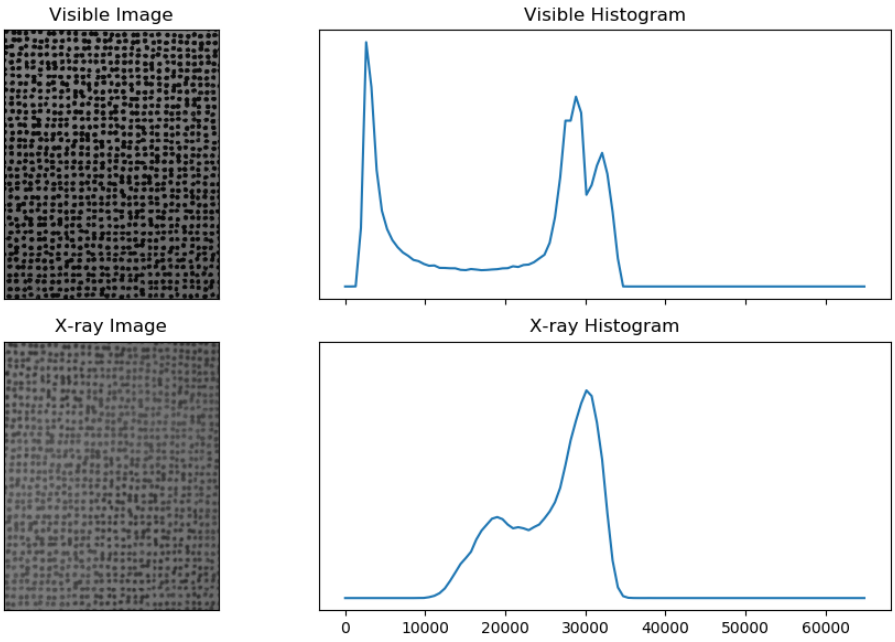

Figure 15: Histogram comparison between visible light and X-ray images. The visible light images have significantly more contrast between the dark speckles and bright background.

5 Imaging System Calibration

Stereo DIC measurements require a calibration process to determine intrinsic parameters, such as lens focal length, image center, and image distortion parameters, as well as extrinsic parameters that describe the relative position of one camera with respect to the other. In sum, these calibration parameters govern the relationship between points on the two images and points in 3D space. For visible light imaging systems, the well-known pinhole camera model is typically employed, and image distortions models are based on those physically induced by lenses and viewport windows. For a first approximation, the X-ray imaging system can employ the same camera and distortion models, thus allowing commercial DIC calibration software developed for visible imaging systems to be employed for X-ray imaging systems. However, there are known deficiencies in the current models when applied for X-ray imaging, such as a missing transformation term describing the alignment of the camera sensor with the scintillator and inability to appropriately account for non-flat or warped scintillators, which are a subject for future work.

5.1 Practical Aspects of X-ray Calibration

Calibration of an X-ray imaging system is practically more difficult than calibration of a visible light imaging system. For a visible light system, the operator can be in the room directly moving the calibration target. The images are relatively noise free, so averaging images is not necessary; the calibration can be uncontrolled and performed in one pass. Acquired images can then be decimated appropriately and saved to disk also in one pass. While keeping bright lights on for an extended period of time can cause the calibration target to heat up and produce heat waves that can distort images, the calibration process is usually fast enough that this is not a problem.

For the X-ray system, the operator typically cannot be in the room with an active X-ray source, and therefore cannot be manipulating the calibration target directly. X-ray images tend to be noisier, so it is generally necessary to average images together to reduce noise inherent in the imaging process. The X-ray on-time needs to be managed to avoid excess heat build-up in the X-ray source, so pauses in calibration may be necessary to allow the system to cool down. For high-speed cameras specifically, these requirements will generally mean that the camera will fill its memory prior to acquiring all calibration images, which will require downloading images in multiple passes.

Initial efforts to perform X-ray calibration took several hours, whereas the visible light calibration can typically be performed in

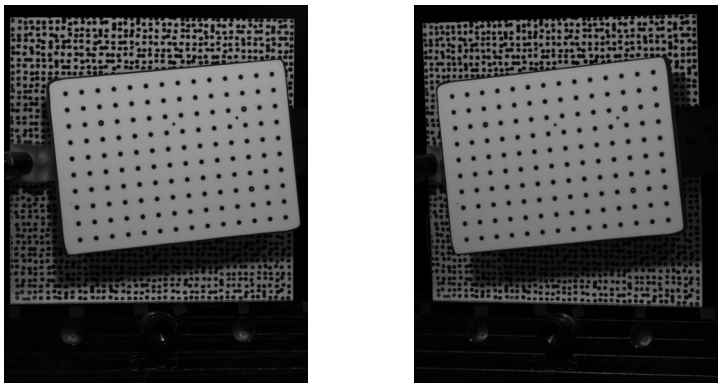

(a) **(b)**

Figure 16: Representative stereo calibration images for the visible light imaging system

a few minutes. For this reason, a more automated calibration strategy was sought. Motorized Newmark Rotary and Translational stages were used to position the calibration target in the field of view and control its position remotely. A Python script was written to control the calibration. The `pyphantom` module was used to start and stop the camera acquisition, while the `pyvisa` module was used to interact with a Keysight function generator to supply the trigger signal to the X-ray sources and cameras. The `pyphantom` module was then used to directly read the camera memory to find the images where the X-ray sources were active based on a brightness threshold. These images were downloaded and averaged to produce a final calibration image for a single calibration target position. The Python script then moved the stages to the next position and the process was repeated.

5.2 Visible Light Calibration Results

Visible light calibration was performed using a standard Correlated Solutions dot grid target with 14×10 dots spaced 7 mm apart. Calibration images were acquired with the actual test settings described in subsequent sections while the target was rotated and translated by hand. Acquired images were decimated to keep approximately 100 image pairs. A standard calibration model with fixed aspect ratio, no skew parameters, and 2 radial distortion parameters was used. Calibration was performed in the VIC3D software, and a calibration score of 0.022 was achieved. Figure 16 shows a representative pair of stereo calibration images for the visible light imaging system. Note that while ideally the calibration would ideally be performed over the entire measurement volume, this was not feasible for this test. Removing and installing the plate for calibration each day changed boundary conditions, and handling the plate was avoided to prevent damaging the speckles. In addition, due to the tight test setup, it was difficult to adjust the camera field of view if the plate shifted slightly. Therefore, the calibration was performed with the target in front of the test plate. Understanding that this trade-off could reduce the calibration accuracy, the calibration score and reprojection error were checked prior to acquiring test images.

5.3 X-ray Calibration Results

For X-ray calibration, the dots on the calibration target are required to have some material contrast compared to the background. The calibration target used in this test was a printed circuit board with copper circles embedded in the board. A 9×9 grid was used with 15 mm grid spacing. The target is shown mounted to a portion of the rotation stage in Figure 17. Images were acquired every 5° rotation about the vertical axis at three linear positions along the depth direction and at three tilts about the horizontal axis. 100 images were captured and averaged at each stage position to reduce noise. Images were flipped horizontally, light-field corrected, and histogram re-ranged to aid the dot-finding algorithm in the VIC3D software. The calibration model used was a standard model with free aspect ratio, skew, and 3 radial, 2 tangential, and 2 prismatic distortion terms. The calibration was performed using the VIC3D software, and a calibration score of 0.074 was achieved. Figure 18 shows a representative stereo pair of X-ray calibration images along with the X-ray correction steps.

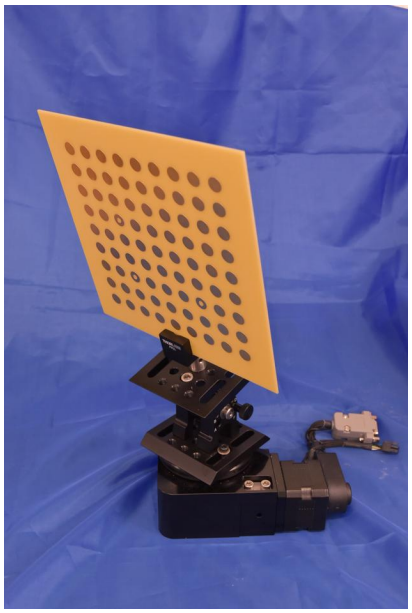

Figure 17: X-ray calibration target mounted to a portion of the rotational stage.

5.4 Hybrid Calibration

The VIC3D software gives users the capability to perform a hybrid calibration that supplements the initial calibration with speckle pattern images. This approach was used here to try to improve the calibration results. Correlation between left and right stereo images provides consistent sets of image points that can be used to refine the initial dot-grid calibration: the positions on the speckle pattern image can generally be found with greater accuracy than the extracted dot centers of a standard dot-grid calibration target, and the speckle pattern also provides more points to calibrate from compared to the number of dots on a calibration target. The test article was mounted to a translational stage similarly to the calibration target, and images were acquired using both imaging systems.

Using the hybrid calibration, X-ray calibration score improved from 0.074 to 0.023. Interestingly, when applied to the visible light calibration, the calibration score worsened from 0.022 to 0.2, but the reprojection error dropped from 0.14 to 0.01, so it was thought that the calibration was still improved despite the reported calibration score worsening.

6 Dynamic Experiments

The goal of the dynamic experiment is to perform a standard experimental modal test using shaker excitation, measuring drive point data with a force gauge and accelerometer, and then merging those data with the DIC measurements from either the visible light or X-ray imaging systems. Tests were run at five shaker excitation levels to observe how the results of the visible and X-ray DIC compare as displacement values were decreased from clearly visible to nearly imperceptible vibration levels. The dynamic test parameters are shown in Table 4. Note that while 10 averages were planned, the uncertainty in the X-ray source anode spin-up time meant that a full 10 averages could not be acquired within the time limit provided by the X-ray software; only 9 full measurement frames could be reliably acquired.

6.1 DIC for Experimental Modal Analysis

The general DIC – Experimental Modal Analysis workflow is as follows. Visible light and X-ray images are exported from the cameras. Because the excitation is periodic, image averaging can be performed across measurement frames to reduce noise on the images as well as reduce the number of images that must be processed in the DIC software. The averaged X-ray images are light-field corrected, and both averaged image sets are loaded into the VIC3D software for analysis. Analysis parameters are shown in Table 5, and representative subset sizes are shown in Figure 19. Raw displacements are exported to `.mat` files for post-processing. The `.mat` files are loaded into a custom Python script that extracts test geometry and formats displacement time

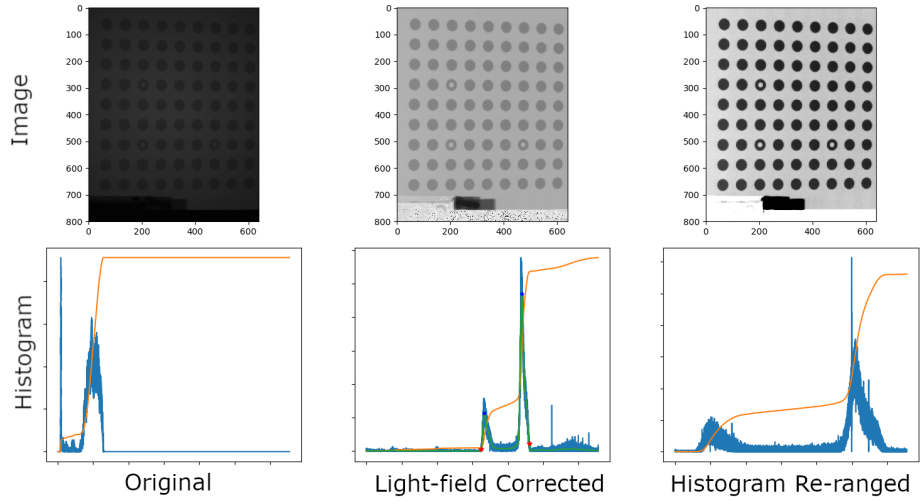

(a) Left system

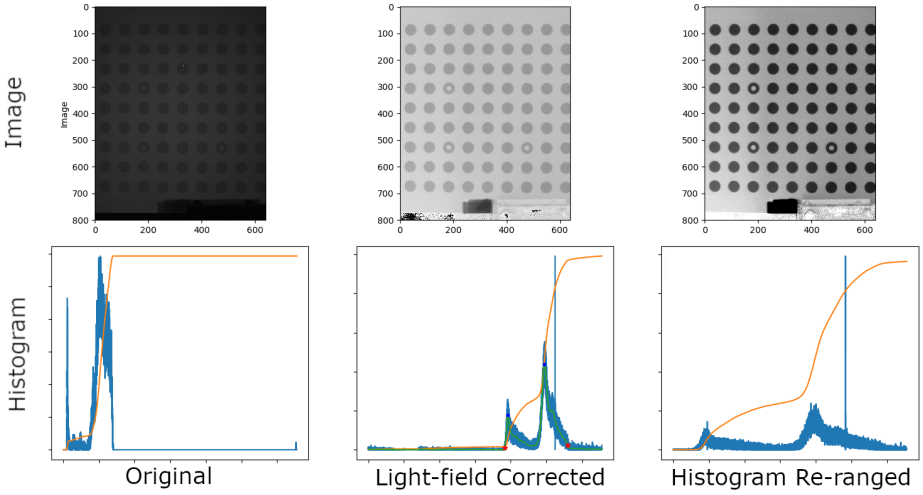

(b) Right system

Figure 18: Representative stereo calibration images for the X-ray imaging system showing effect of light-field correction and histogram re-ranging

.

Table 4: Test parameters for the dynamic modal test.

System:	Visible Light Cameras	X-ray Cameras	Modal DAS
Make/Model	Phantom v1212	Phantom v2511	B&K LAN XI
Lens	Nikon Nikkor 105mm	Zeiss Distagon 35 mm	–
Aperture (f/#)	11	1.4	–
Resolution (px,px)	640 x 800	640 x 800	–
Exposure Time (us)	240	240	–
Sample Rate (Hz)	4096	4096	8192
Frame Length (s)	0.5	0.5	0.5
Frame Averages	9	9	9
Samples Taken	18432	18432	36864
Frequency Resolution (Hz)	2	2	2
Pre A/D High-Pass Filter (Hz)	–	–	1
Windows	–	–	None

Excitation	
Type	Pseudorandom
Input Range (Hz)	10-1000
Stinger Length (in)	3
Input Force (lbf RMS)	0.01 - 0.13
X-ray System	
Source Housing	Varex B-147
Source Tube	Varex G-292
Focal Spot (mm)	1.2
Voltage (kV)	130
Current (mA)	100
Pulse Duration (ms)	100
Scintillators	GOS:Pr

Table 5: DIC parameters used for all analyses described in this work.

DIC Analysis Settings	
Images	16 bit TIFF Γ=1.0 Average images prior to DIC
Software	Correlated Solutions VIC-3D v8
Subset Size (px,px)	51 x 51
Step Size (px)	25
Nominal Subset Count	420
Approximate Features/Subset	16 (4x4)
Subset Weights	Gaussian
Interpolant	Optimized 8-tap
Correlation Criterion	Zero-normalized sum square differences
Image Low-pass Filtering	No
Incremental Correlation	No
Fill Boundary	No
Use Left Stereo Reference	No
Exhaustive Search	No
Coordinate System	Default (transform in post processing)

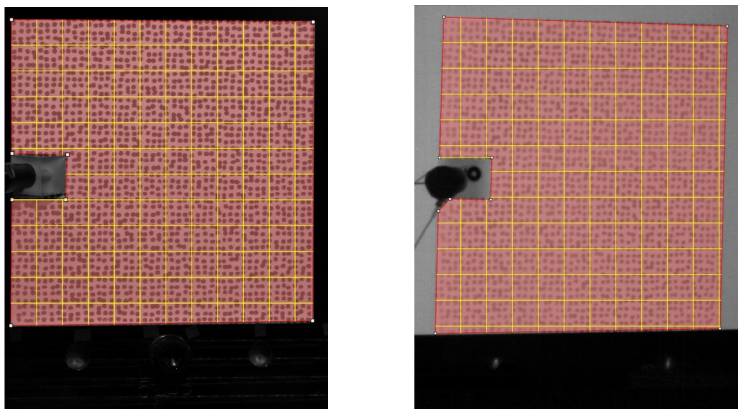

(a) Visible light image **(b)** X-ray image

Figure 19: Representative test images with area of interest and subset size overlay.

histories while computing uncertainty metrics and showing quick-look plots. These data are then exported to a format readable by the Synthesize Modes and Correlate (SMAC) [4] curve fitting software and merged with the drive point acceleration and force data. Frequency response functions (FRFs) can then be computed from this combined dataset. The FRFs are then analyzed using SMAC to extract modes.

One interesting lesson learned for future testing was the effect of the X-rays on the force and accelerometer measurements, shown in Figure 20. Especially in the acceleration signal, there are obvious voltage spikes when the X-ray sources are activated and deactivated. A 10 Hz high-pass filter was able to remove the spike and provide data that could be used for modal analysis.

6.2 Comparing Modal Results

Modal parameters extracted from the X-ray and visible light tests are compared directly. To facilitate shape comparisons, the visible light mode shapes, which are generally smoother, are interpolated to the X-ray subset positions, and the Modal Assurance Criterion (MAC) was computed between the visible light and X-ray shapes.

To develop a shape noise metric, experimental shapes Φ_{EXP} were smoothed using the System Equivalent Reduction Expansion Process (SEREP) [5] using a plate finite element model with shapes Φ_{FEM}. Residuals were computed by subtracting the

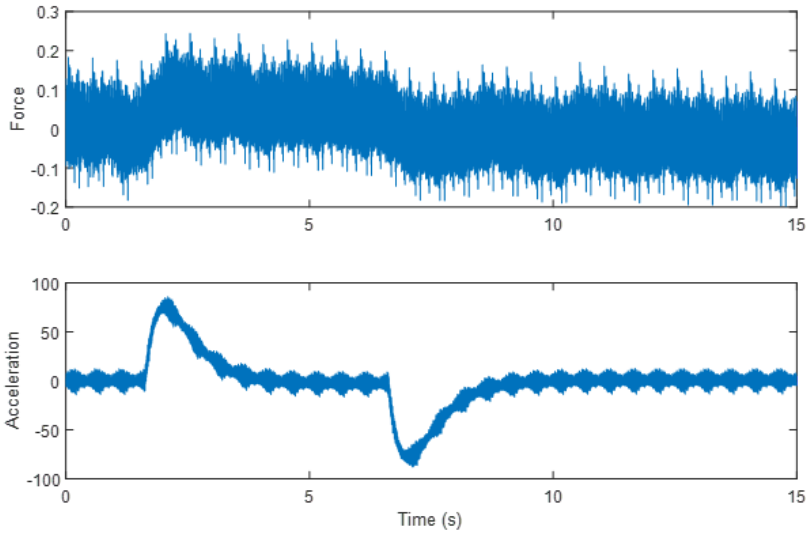

Figure 20: Effect on the measured acceleration and force signals due to starting and stopping the X-ray system.

measured shape from the smoothed shape, with some representative smoothing results shown in Figure 21. A normalized noise metric ε_{shape} was computed as the RMS of the residual displacement divided by the RMS of the smoothed shape's displacement.

$$\varepsilon_{shape} = \frac{\mathrm{RMS}(\Phi_{\mathrm{EXP}} - \Phi_{\mathrm{FEM}}\Phi^{+}_{\mathrm{FEM}}\Phi_{\mathrm{EXP}})}{\mathrm{RMS}(\Phi_{\mathrm{FEM}}\Phi^{+}_{\mathrm{FEM}}\Phi_{\mathrm{EXP}})} \tag{1}$$

Modal filtering was performed to separate the measured response into individual modes, with a representative result shown in Figure 22. By passing the per-mode displacements through the camera equations, it is possible to compute the number of pixels of displacement per mode shape to better understanding the relationship between the on-image displacement of a given mode and the level of noise on that shape.

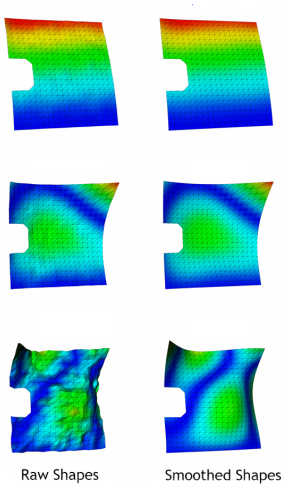

Figure 21: Shape smoothing using SEREP to develop a shape noise metric.

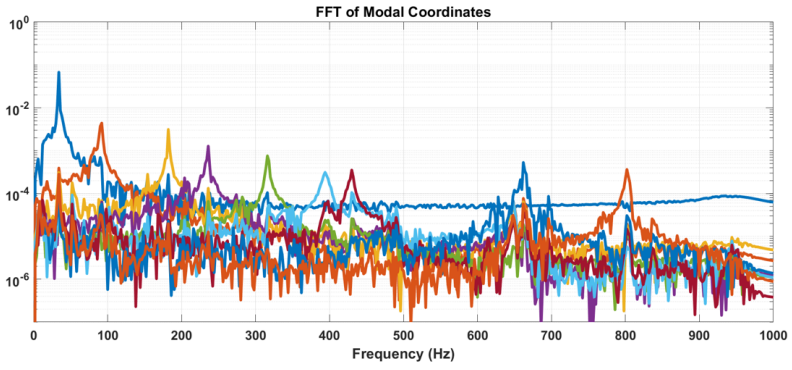

Figure 22: Displacement spectra for each mode in a representative test.

6.3 Dynamic Results

This section contains the results from the dynamic experiments. Five levels were tested, with the highest, middle, and lowest levels reported in this document. Modal parameters are tabulated in Tables 6–8 along with RMS pixel displacement values from the modal filtering and the shape noise metrics. Complex Mode Indicator Functions (CMIFs) showing a comparison between the test data and modal reconstruction are shown in Figures 23, 26, and 29 so the reader can judge the adequacy of the fit as well as get an idea of how far each peak was above the measurement noise floor. The extracted mode shapes are shown in Figures 25, 28, and 31. MAC matrices are shown in Figures 24, 27, and 30.

6.3.1 High Level Results

High level results were obtained using a shaker excitation of 0.58 N RMS. For this test, there is very good agreement between natural frequencies, with slightly larger errors between the very light critical damping ratios. Because of the damping differences, the modal scale factor (MSF) between the two sets of shapes can be off; however, the MAC shows good shape agreement across the bandwidth. For this test, the low frequency modes saw almost 1 pixel RMS of displacement, while the high frequency modes saw only a few hundredths of a pixel RMS. The noise metrics showed similar noise levels between the two sets of shapes until about 400 Hz, after which the X-ray shapes showed significantly more noise. This noise is clearly visible on last three X-ray shapes shown in Figure 25.

Table 6: Comparison of modal parameters extracted at a high excitation level.

Flat Force Pseudorandom (-18dB, Run 41)												
Mode	Frequency			% Crit Damping			MSF	MAC	Visible Peak Px RMS	Xray Peak Px RMS	Visible Noise	Xray Noise
	Visible	Xray	%Diff	Visible	Xray	%Diff						
1	34.00	34.15	0.45	0.62	0.70	12.93	0.86	99.88	0.4663	0.9958	2.28	2.16
2	90.77	90.72	-0.05	0.58	0.75	28.90	1.12	99.58	0.0844	0.1815	5.14	6.72
3	181.45	181.55	0.05	0.49	0.47	-3.11	1.13	99.63	0.0381	0.1009	6.00	6.74
4	231.30	231.54	0.10	0.95	0.93	-2.54	1.16	99.69	0.0404	0.0851	5.11	6.21
5	314.63	314.63	0.00	0.47	0.42	-10.44	1.12	99.61	0.0184	0.0435	8.00	9.11
6	393.61	393.96	0.09	1.34	1.17	-12.18	1.13	99.51	0.0121	0.0249	5.76	7.54
7	426.85	428.35	0.35	0.50	0.12	-75.02	2.13	97.92	0.0100	0.0231	5.24	12.71
8	654.98	654.33	-0.10	0.20	0.07	-62.91	1.21	93.67	0.0063	0.0203	6.95	23.09
9	795.59	794.79	-0.10	0.41	0.37	-9.26	0.94	97.11	0.0083	0.0195	6.68	15.29

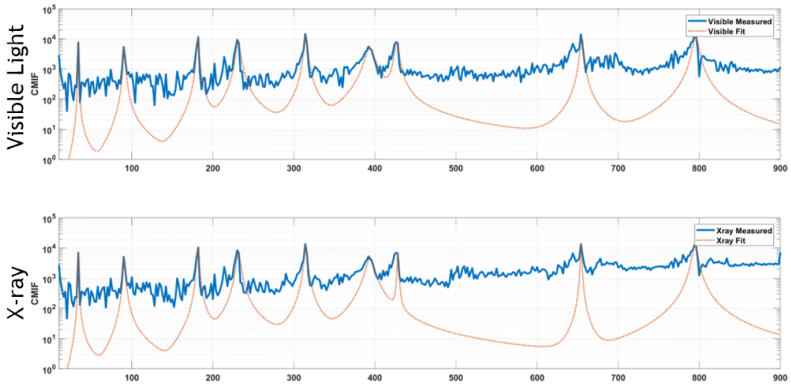

Figure 23: Modal fits for the high excitation level test.

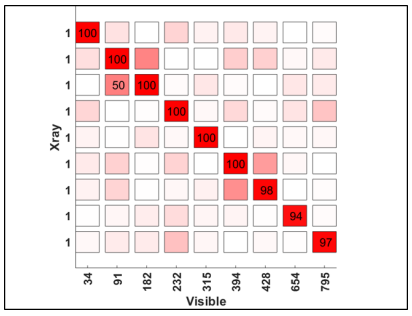

Figure 24: MAC between shapes extracted from the high level test.

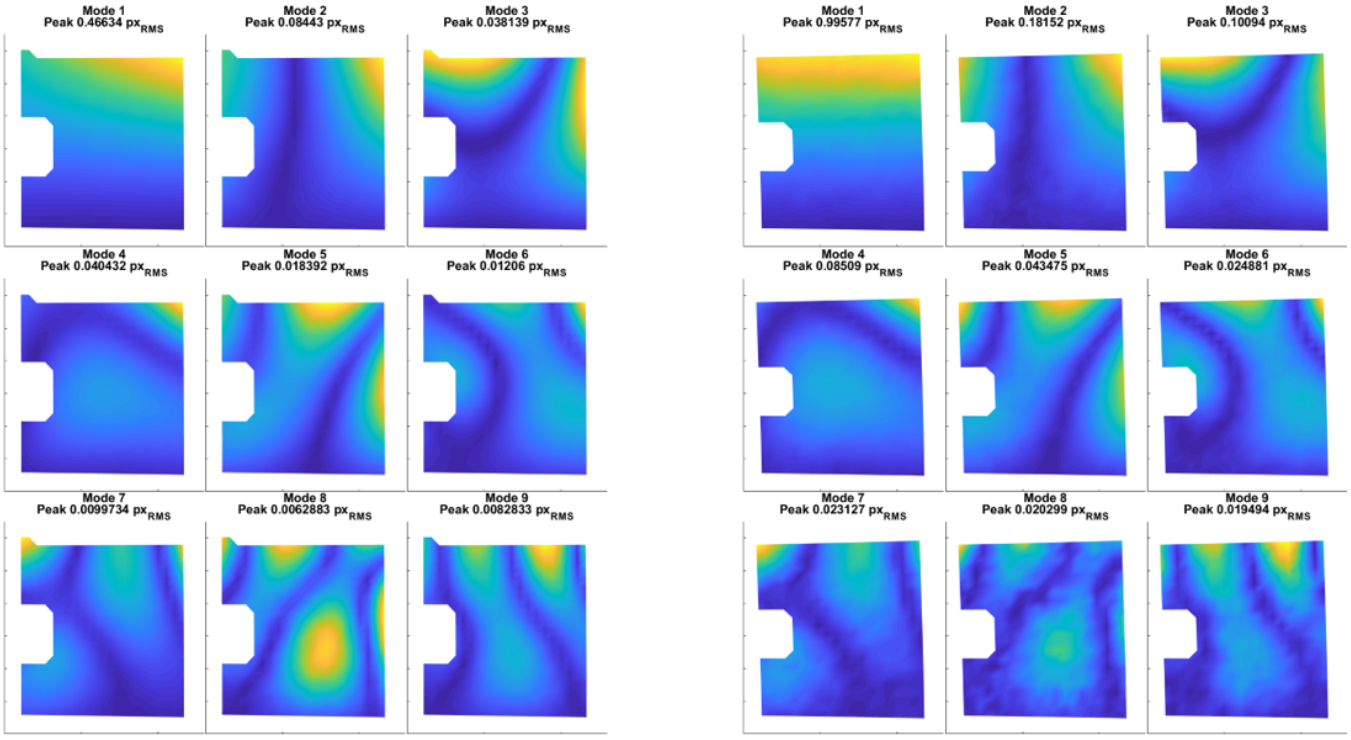

(a) Visible Light

(b) X-ray

Figure 25: Shape comparison for the high level test.

6.3.2 Mid-Level Results

The middle test level was approximately 4 times lower than the high test level with a shaker excitation of 0.16 N RMS. For this test, the noise floor of the X-ray measurement starts to bury the high frequency modes, which is clearly visible in Figure 26. The natural frequencies are still reasonably extracted, likely due to the presence of the drive point accelerometer measurement; however, with RMS pixel displacements of less than one hundredth of a pixel, the extracted shapes are very noisy. The MAC comparisons between visible light and X-ray shapes drop below 90% for many of the modes in the frequency band.

Table 7: Comparison of modal parameters extracted at a medium excitation level.

Flat Force Pseudorandom (-30dB, Run 44)												
Mode	Frequency			% Crit Damping			MSF	MAC	Visible Peak Px RMS	Xray Peak Px RMS	Visible Noise	Xray Noise
	Visible	Xray	%Diff	Visible	Xray	%Diff						
1	34.20	34.03	-0.50	0.35	0.26	-27.73	2.31	99.83	0.0443	0.0937	2.90	3.10
2	91.31	91.22	-0.10	1.17	0.71	-39.17	1.05	98.63	0.0252	0.0430	5.17	10.18
3	181.27	181.27	0.00	0.43	0.36	-16.26	1.08	97.41	0.0100	0.0240	6.32	13.72
4	231.54	231.54	0.00	0.70	0.65	-7.68	1.10	98.02	0.0104	0.0203	5.37	12.54
5	315.21	314.89	-0.10	0.53	0.39	-26.31	1.04	97.00	0.0045	0.0088	8.37	14.07
6	389.80	389.22	-0.15	0.83	0.49	-40.60	1.16	92.22	0.0036	0.0070	6.47	25.96
7	425.79	423.76	-0.48	0.89	0.60	-32.46	0.91	84.24	0.0025	0.0045	5.81	34.86
8	655.02	654.69	-0.05	0.40	0.09	-76.58	0.69	57.77	0.0018	0.0032	8.52	69.35
9	795.59	796.03	0.06	0.36	0.13	-64.80	0.87	48.98	0.0022	0.0029	8.41	81.06

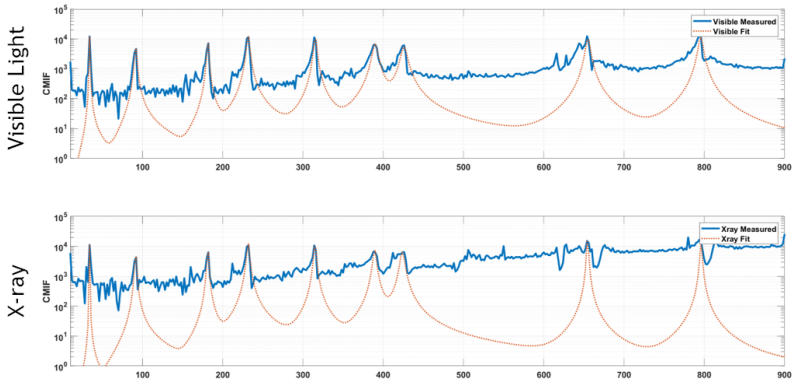

Figure 26: Modal fits for the medium excitation level test.

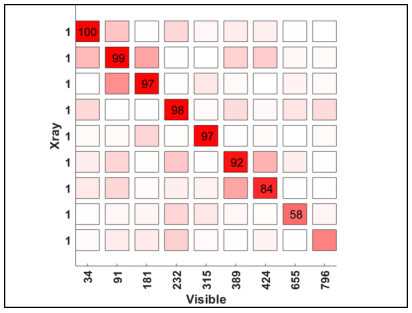

Figure 27: MAC between shapes extracted from the medium level test.

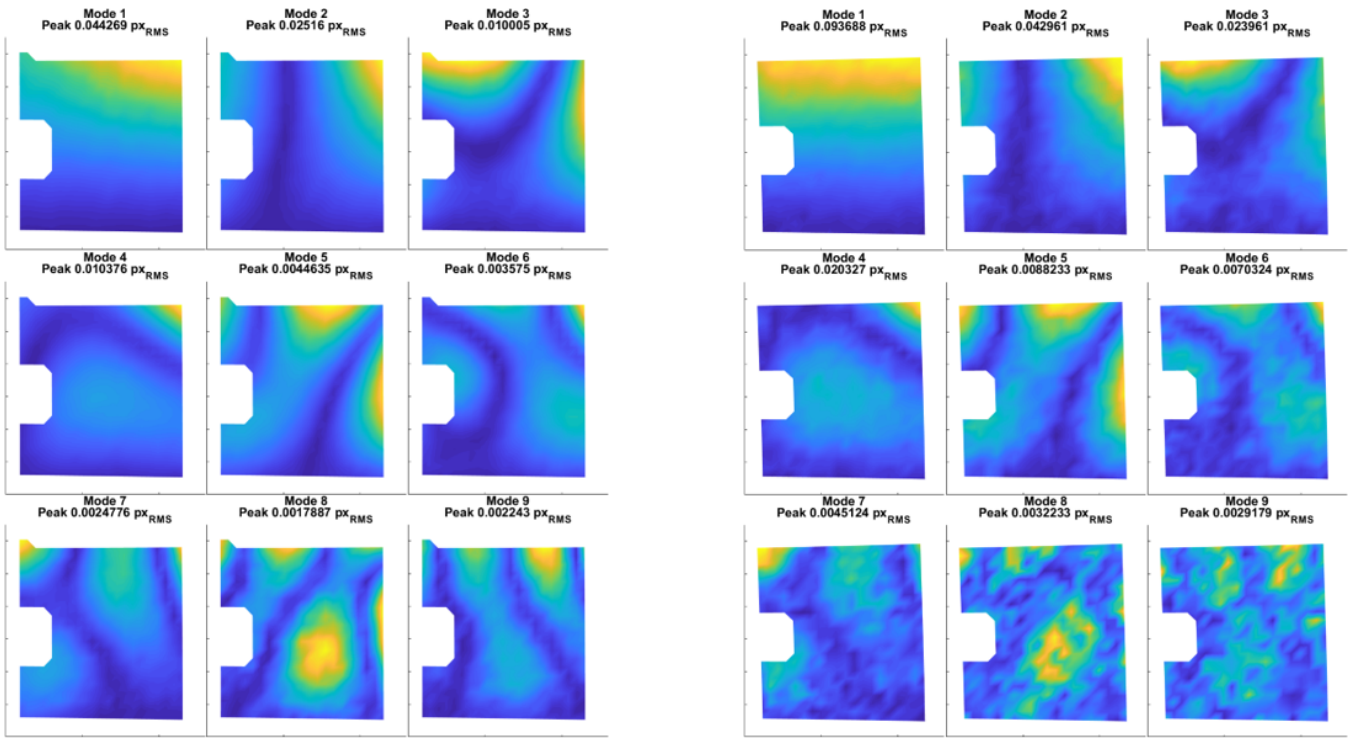

(a) Visible Light

(b) X-ray

Figure 28: Shape comparison for the medium level test.

6.3.3 Low Level Results

The low level test was again approximately 4 times lower than the middle test level with a shaker excitation of 0.048 N RMS. For this test, all but the first X-ray mode shape show significant noise. Even the shapes extracted from the visible light test have started to show significant degradation, due to only having a few thousandths of a pixel RMS displacement on the image.

Table 8: Comparison of modal parameters extracted at a low excitation level.

Flat Force Pseudorandom (-42dB, Run 42)												
Mode	Frequency			% Crit Damping			MSF	MAC	Visible Peak Px RMS	Xray Peak Px RMS	Visible Noise	Xray Noise
	Visible	Xray	%Diff	Visible	Xray	%Diff						
1	34.07	34.07	0.00	0.26	0.20	-21.75	1.06	99.45	0.0131	0.0260	3.00	6.24
2	90.05	90.09	0.05	0.75	0.77	2.37	0.75	68.72	0.0124	0.0080	6.96	56.39
3	181.18	181.36	0.10	0.28	0.48	74.45	1.09	84.97	0.0085	0.0086	8.90	33.92
4	231.88	231.88	0.00	0.61	0.62	0.79	0.80	70.33	0.0052	0.0079	5.92	57.31
5	315.53	315.53	0.00	0.46	0.44	-4.60	0.86	79.61	0.0015	0.0030	8.80	43.75
6	390.97	389.61	-0.35	0.37	0.02	-94.33	0.21	22.11	0.0039	0.0019	10.38	118.58
7	424.64	424.08	-0.13	0.53	0.01	-97.39	0.33	6.95	0.0023	0.0012	14.45	193.54
8	655.96	656.02	0.01	0.24	0.02	-93.44	0.14	4.16	0.0010	0.0009	33.19	193.26
9	794.78	795.87	0.14	0.33	0.02	-92.60	0.08	1.67	0.0020	0.0012	27.27	249.18

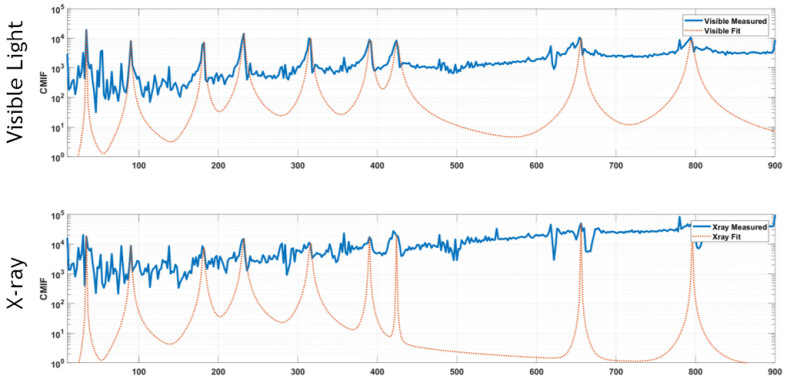

Figure 29: Modal fits for the low excitation level test.

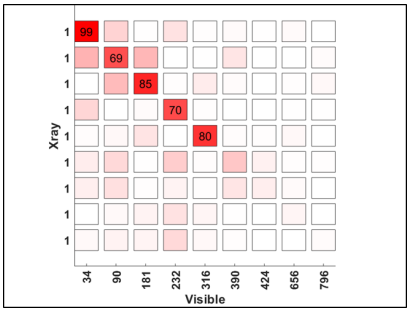

Figure 30: MAC between shapes extracted from the low level test.

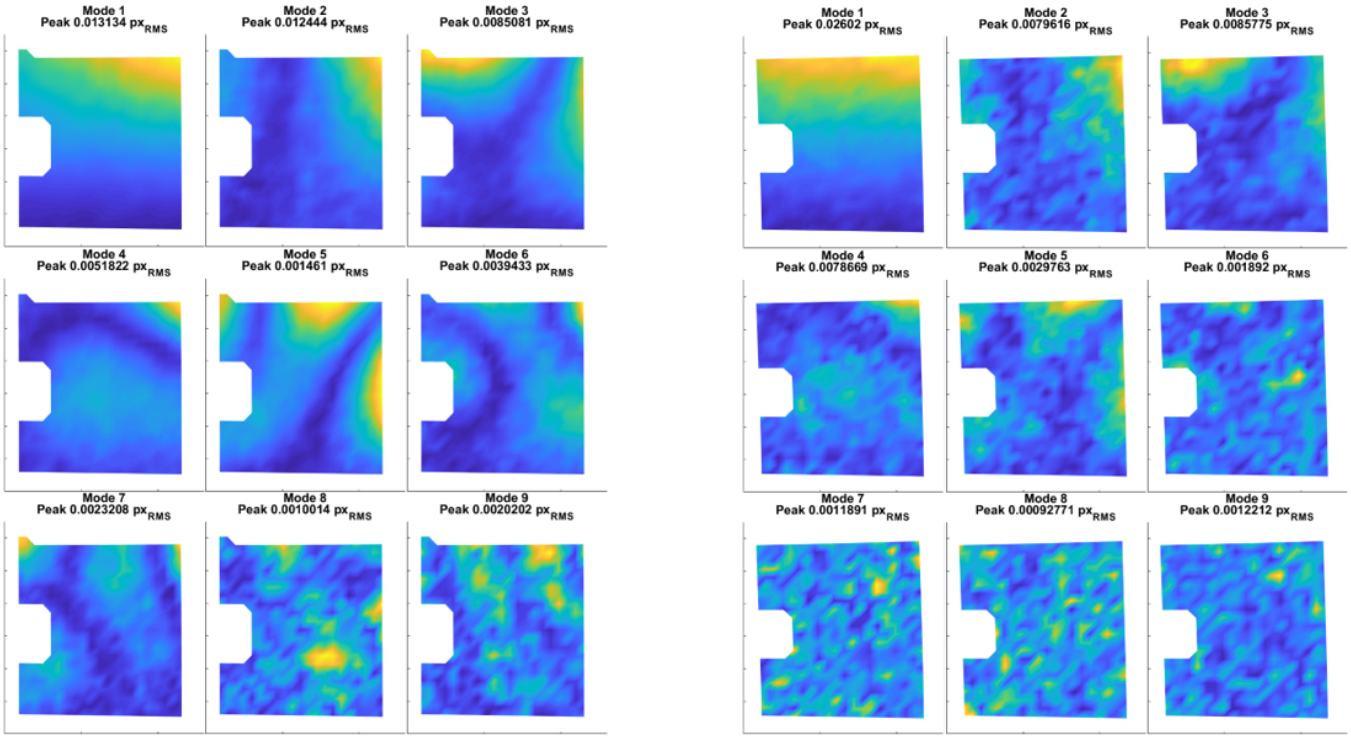

(a) Visible Light **(b)** X-ray

Figure 31: Shape comparison for the low level test.

7 Summary of Test Results

Combining all extracted mode shapes over all dynamic test levels reveals insights into the imaging techniques. Figure 32 shows the MAC between the X-ray and visible light shapes plotted against the shape noise metric used in this paper for X-ray images. The distribution is surprisingly tight considering the dataset contains different shapes at different frequencies and different excitation levels. This distribution allows us to develop a relationship between the MAC and the shape noise. For example, if a MAC of 0.9 is desired, a shape noise metric of less than 27 is required. We can then plot this noise metric against the RMS pixels of displacement for each mode for each test level to determine trends between pixels of displacement and shape noise, and gain intuition regarding what level of displacement is required to reasonably extract a given mode for a given test type. Visible light shapes are consistently below the noise threshold out to approximately 0.001 RMS pixel displacement. The X-ray shapes are below this threshold until approximately 0.01 RMS pixel displacement.

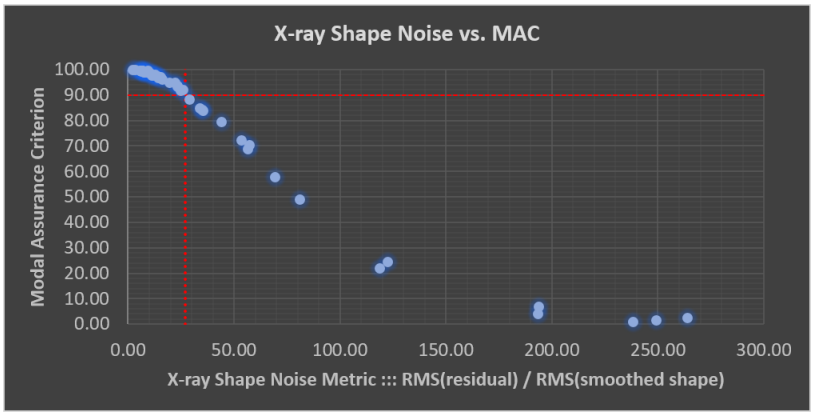

Figure 32: MAC compared to the Shape Noise Metric used in this paper for all shapes extracted at all excitation levels. A MAC of 90% clearly corresponds to a shape noise metric of 27.

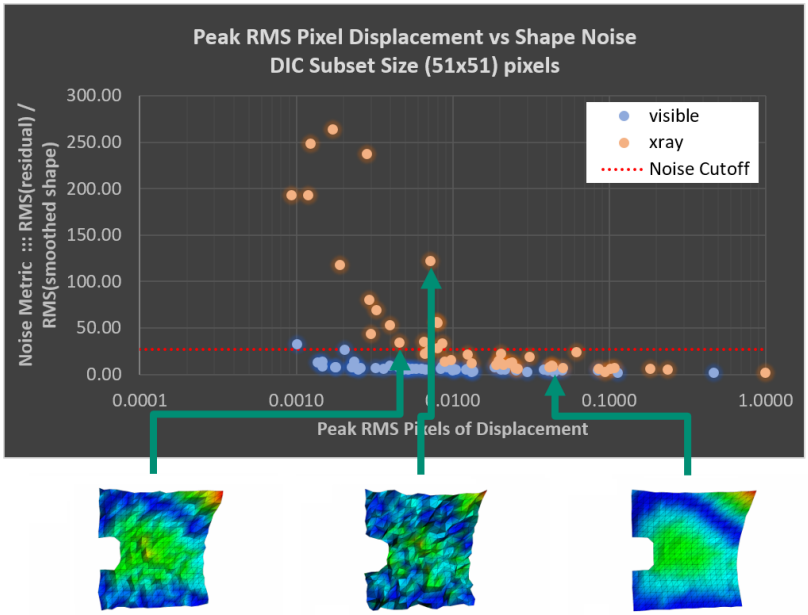

Figure 33: Pixel displacement compared to the noise metric with cutoff of 27 shown. Three X-ray shapes corresponding to elastic mode 4 from varying test levels are shown to aid in visualizing the noise level corresponding to a given shape noise metric.

8 Conclusions

The dynamic testing presented in this paper showed that both X-ray and visible light images could be used to perform experimental modal analysis to extract dynamics information from a test article. This is a major step towards developing image-based measurement techniques that can extract full-field motions from both internal and external surfaces of a test article.

8.1 Summary of Differences between X-ray and Visible Light

A number of practical considerations made X-ray DIC testing significantly more challenging than testing with visible light. Speckling was much more difficult for the X-ray test than the visible light test. While a visible light test can simply use paint or a sticker, material had to be added or removed from the part to create contrast for the X-ray system. This makes it much more difficult to achieve an optimal contrast pattern. The power requirements and limited ability to dissipate heat in the X-ray source resulted in the inability to use the optimal power settings for the dynamic X-ray test, which further limited the contrast available in the X-ray images.

Calibration was another portion of the test that was significantly more difficult in the X-ray case. Luckily, the relatively large mass of the X-ray sources and secure mounting of the X-ray cameras and scintillators provided a stable imaging setup that would generally hold its calibration for several days. With the X-ray system requiring several hours to calibrate, it was not feasible to calibrate every day prior to testing, which is a recommended practice for standard DIC measurements with visible light. It was found that existing camera models could be used for X-ray calibration, so existing DIC software could be used directly without major modifications. However, if there is warping in the scintillators or significant lens distortions in the X-ray cameras, a new camera model may be required to accommodate those issues.

The simultaneous visible light and X-ray imaging did complicate the test setup. As this was the first attempt to perform X-ray imaging of a modal test, it was important to have a more standard measurement technique to compare against. However, some of these difficulties would be alleviated if performing only an X-ray measurement.

8.2 Future Work

DIC is a thoroughly vetted image processing technique that has become the industry standard for extracting motions from images. However, the utility of DIC is expected to be reduced as the radiographic imaging scenarios become more complex. For example, if one would wish to measure the response of an internal component along with the exterior of a part with radiographic techniques, one would need to put a speckle pattern both on the internal component as well on the external surface. DIC is expected to struggle in a scenario like this. Parallax effects will result in a different portion of the internal component being behind the same portion of the external surface for two different views of the same test article. This will make it difficult for DIC to perform the cross correlation between the stereo image pair. Additionally, if the internal component moves opposite the external surface, the speckle pattern will appear to morph rather than translate, and it may be difficult to track the internal and external surfaces independently.

One solution to this issue is to use a simultaneous visible light and X-ray test, like was performed in this work, where the visible light system would measure the external surfaces while the radiographic component would measure the internal components.

An alternative approach is to use other image processing approaches. Phase-based processing [6, 7] has been shown to have a lower noise floor than traditional DIC, and due to the filtering of the image over multiple spatial scales and orientations, it can extract multiple motions at a single pixel, which could prove useful for radiographic imaging where some internal component might be moving opposite some external surface. A limitation of the approach is that motions can only be extracted where there is contrast on the image. However, recent work has shown the ability to perform finite element expansion on image degrees of freedom to predict measured responses [8]. This has recently been extended to phases from phase-based processing approaches [9]. Finite element expansion can therefore be used to fill in the gaps in the low contrast regions of radiographic images.

Another avenue of research is performing computed tomography (CT) to extract motions from radiographic images. Traditional CT requires imaging of a component from many different angles, and incorporating this into a modal test would require each of those angles to be captured at each time step. This could theoretically be achieved with a periodic excitation and a very long-running test; however, a more feasible approach being pursued by Sandia National Laboratories is to build up a multi-view X-ray system so many views can be acquired simultaneously.

References

[1] E. M. C. Jones, E. C. Quintana, P. L. Reu, and J. L. Wagner, "X-ray stereo digital image correlation," *Experimental Techniques*, vol. 44, pp. 159–174, Apr. 2020.

[2] B. L. Witt, J. J. Wilbanks, B. C. Owens, and D. P. Rohe, "Stereo photogrammetry camera pose optimization," in *Proceedings of the 39th International Modal Analysis Conference*, (Virtual), Feb. 2021.

[3] E. M. C. Jones and M. A. Iadicola, eds., *A Good Practices Guide for Digital Image Correlation*. International Digital Image Correlation Society, Oct. 2018. doi: https://doi.org/10.32720/IDICS/GPG.ED1.

[4] R. L. Mayes and S. E. Klenke, "The SMAC modal parameter extraction package," Sandia Report SAND98-2366C, Sandia National Laboratories, Sandia National Laboratories, Albuquerque, NM 87185, 1998.

[5] J. C. O'Callahan, P. Avitable, and R. Riemer, "System equivalent reduction expansion process," in *Proceedings of the Seventh International Modal Analysis Conference*, (Las Vegas, NV), Feb 1989.

[6] N. Wadhwa, M. Rubinstein, F. Durand, and W. T. Freeman, "Phase-based video motion processing," *ACM Trans. Graph.*, vol. 32, pp. 80:1–80:10, July 2013.

[7] A. Molina-Viedma, L. Felipe-Sesé, E. López-Alba, and F. Díaz, "3D mode shapes characterisation using phase-based motion magnification in large structures using stereoscopic dic," *Mechanical Systems and Signal Processing*, vol. 108, pp. 140 – 155, 2018.

[8] D. P. Rohe, B. L. Witt, and T. F. Schoenherr, "Predicting 3d motions from single-camera optical test data," *Experimental Techniques*, pp. 1–15, 2020.

[9] D. P. Rohe, "Computing displacements from phase quantities," in *Proceedings of the 39th International Modal Analysis Conference*, (Virtual), Feb. 2021.